



# 2D quasiperiodic plasmonic crystals

Christina Bauer, Georg Kobiela & Harald Giessen

4<sup>th</sup> Physics Institute and Research Center SCoPE, University of Stuttgart, 70550 Stuttgart, Germany.

## CONFERENCE PROCEEDINGS

Symposium N + O  
E-MRS 2012  
Spring Meeting  
.....

SUBJECT AREAS:  
OPTICS AND PHOTONICS  
MATERIALS SCIENCE  
NANOPARTICLES  
SPECTROSCOPY

Received  
3 July 2012

Accepted  
5 September 2012

Published  
3 December 2012

Correspondence and  
requests for materials  
should be addressed to  
C.B. (c.bauer@pi4.uni-  
stuttgart.de)

Nanophotonic structures with irregular symmetry, such as quasiperiodic plasmonic crystals, have gained an increasing amount of attention, in particular as potential candidates to enhance the absorption of solar cells in an angular insensitive fashion. To examine the photonic bandstructure of such systems that determines their optical properties, it is necessary to measure and model normal and oblique light interaction with plasmonic crystals. We determine the different propagation vectors and consider the interaction of all possible waveguide modes and particle plasmons in a 2D metallic photonic quasicrystal, in conjunction with the dispersion relations of a slab waveguide. Using a Fano model, we calculate the optical properties for normal and inclined light incidence. Comparing measurements of a quasiperiodic lattice to the modelled spectra for angle of incidence variation in both azimuthal and polar direction of the sample gives excellent agreement and confirms the predictive power of our model.

Coupled systems play a major role in nanophotonics and plasmonics. Plenty of applications such as optical nanosensors<sup>1–3</sup> are based on Fano resonances<sup>4</sup> which are due to interactions of different optical modes. The influence of planar periodic structures on particle plasmon resonances was studied by Lamprecht et al.<sup>5</sup> and Auguie et al.<sup>6</sup> Subwavelength holes in a metal film have been investigated by Garcia-Vidal and coworkers<sup>7</sup>. All of the mentioned publications have only examined periodic structures. However, also planar aperiodic and disordered structures have been studied<sup>8–11</sup>. Even 3D photonic quasicrystals were investigated<sup>12,13</sup>. The coupling between particle plasmons and waveguide modes has been studied in periodic<sup>14–16</sup> as well as in disordered<sup>17–19</sup> systems. Additionally, nonlinear experiments have been performed<sup>20–22</sup>. These systems are used for intriguing applications such as enhancing the efficiency of solar cells<sup>23,24</sup> as well as subwavelength focusing of light<sup>25</sup>. The latter application is based on a quasiperiodic structure. One of the key properties of such quasicrystal-line systems is its more isotropic optical behaviour in comparison with periodic structures<sup>26</sup>. Therefore, the ability to model normally incident as well as angle-dependent optical properties is crucial. However, Fourier-periodic methods such as scattering-matrix calculations cannot predict the spectra of quasiperiodic and disordered structures. Therefore, the presented model of a previous paper for 2D plasmonic gold nanodot arrays on a slab waveguide for normal incidence<sup>27</sup> has to be modified and expanded for oblique light incidence. Our model utilises the Fourier transform of the spatial lattice positions in combination with the dispersion of the slab waveguide. Additionally, elliptically shaped nanodots are taken into account. Experiments with different incident polarisations, different inclination angles as well as different azimuthal angles are compared to the theoretical curves, and excellent agreement is obtained. With the model presented in this paper, predictions of the optical properties of structures with a quasiperiodic gold disk arrangement are possible, which is confirmed by experiments. Therefore, the optical properties of future applications of these structures can be modelled and optimized by using this approach. Such applications include for example plasmon-assisted coatings for solar cells which would make their absorption more isotropic and polarisation insensitive.

## Results

**Modelling and simulations.** In the model as well as the experiment, a sample is used which consists of a 180-nm-thick HfO<sub>2</sub> slab waveguide on a quartz substrate with plasmonic gold dots on top, arranged in a quasicrystalline Penrose tiling (see Fig. 1 and **Methods** for details). Light with the vector  $\mathbf{k}$  incident on the sample is defined by the angle of incidence  $\vartheta$  as well as the azimuth angle  $\varphi$  [see Fig. 2(a)]. In comparison with normal light incidence the incident  $\mathbf{k}$  vector additionally possesses components parallel to the  $xy$  plane. Since the electric field vector  $\mathbf{E}_z$  is always perpendicular to  $\mathbf{k}$ ,  $\mathbf{E}_z$  can exhibit a component in  $z$  direction depending on  $\varphi$  and on the polarisation angle  $\alpha$  between the component  $\mathbf{E}_{z,xy}$  and the  $x$  axis of the sample. Therefore, the theoretical model described in Ref. 27 has to be expanded. First, we start by calculating the 2D Fourier transform of the structure. This is carried out by setting a Dirac delta function at each coordinate of the nanodisks<sup>17,27</sup> with  $x_n$  and  $y_n$  for the  $n^{\text{th}}$  disk leading to a function

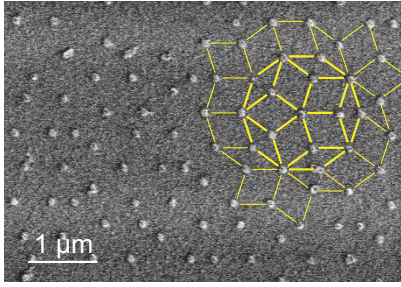


**Figure 1 | SEM picture.** SEM picture of the Penrose tiling of the plasmonic gold nanodots on top of an HfO<sub>2</sub> slab waveguide.

$$f(x,y) = \sum_n \delta(x-x_n)\delta(y-y_n) \quad (1)$$

and then taking the 2D Fourier transform of  $f(x, y)$  by using the projection slice theorem (see Ref. 28 and 29):

$$S_\beta(k_\xi) = \int_{-\infty}^{\infty} \left[ \int_{-\infty}^{\infty} f(\xi,\eta) d\eta \right] e^{-2\pi i \xi k_\xi} d\xi. \quad (2)$$

Due to the structure design, namely a grating on top of a waveguide layer, it is possible to excite the waveguide modes. When a transverse electric (TE) or a transverse magnetic (TM) polarised waveguide mode propagates in the waveguide slab, its energy corresponds to a propagation constant  $\beta_p$  defined by<sup>30</sup>

$$\beta_p = \mathbf{k}_{xy} + \mathbf{g} \quad (3)$$

with  $\mathbf{g}$  describing the location of the Fourier components. This indicates that, in order to calculate the angular propagation constants, it is possible to shift the 2D Fourier transform by the  $\mathbf{k}$  component parallel to the  $xy$  plane,  $\mathbf{k}_{xy}$ , which is displayed as vectorially shifted circles in Fig. 2(b). However, each Fourier component as well as  $\mathbf{k}_{xy}$  are dependent on the energy of the incident light. Therefore, for a specific polar angle  $\vartheta$ , the magnitude of the vector  $\mathbf{k}_{xy}$  is different for each Fourier component. In order to find the correct angular propagation constants, the TE and TM waveguide dispersion relations given in Refs. 31 and 32 have to be used. In these dispersion relations, which are plotted in Fig. 2(c) as black solid (TE) and red dashed (TM) curves, the absolute value of  $\beta_p$  given by

$$\beta_p = \sqrt{k^2 \sin^2(\vartheta)^2 + g^2 + 2k \sin(\vartheta)g \cos(\varphi - \beta_{FT})} \quad (4)$$

is taken. This allows for calculation of  $\beta_p$  in dependence on the corresponding  $k$  value of the incident beam for each Fourier component with distance  $g$  to the centre of the Fourier transform at an angle  $\beta_{FT}$  between the direction of this Fourier component and the  $k_x$  axis. The location of the angular propagation constants can then be easily calculated with Eq. (3). The directions of the waveguide modes are given as vectors starting from the centre of the Fourier transform and pointing to the different angular propagation constants. In each of these directions at angle  $\beta$  a TE as well as a TM mode can be guided, where the TE mode (TM mode) is defined with its electric (magnetic) field vector on a plane perpendicular to the direction of propagation. In order to find the correct amount of TE/TM waves propagating in direction  $\beta$ , the amplitudes of incident light with polarisation  $\mathbf{E}_x$  have to be split into the components [see Fig. 2(d)]

$$C_{TE} = \pm \sqrt{C_{\alpha,xy}^2 \sin^2(\alpha - \beta) + C_{\alpha,z}^2}, \quad (5)$$

$$C_{TM} = C_{\alpha,xy} \cos(\alpha - \beta) \quad (6)$$

with

$$C_{\alpha,xy} = \frac{C_\alpha}{\sqrt{1 - \sin^2(\vartheta)\sin^2(\varphi - \alpha)}} \cos(\vartheta), \quad (7)$$

$$C_{\alpha,z} = -\frac{C_\alpha}{\sqrt{1 - \sin^2(\vartheta)\sin^2(\varphi - \alpha)}} \sin(\vartheta)\cos(\varphi - \alpha). \quad (8)$$

The + sign in Eq. (5) belongs to the case when  $0^\circ \leq \alpha - \beta < 180^\circ$ , whereas the - sign describes the case when  $180^\circ \leq \alpha - \beta < 360^\circ$ .  $C_\alpha$  is a factor that depends on the incident wave. Note that only  $C_{TE}$  is dependent on  $C_{\alpha,z}$  due to the fact that  $\mathbf{E}_{\alpha,z}$  is always on a plane perpendicular to the direction of propagation. For dielectric nanodisks these are the only waves propagating in the waveguide and, therefore, the total intensity of the waveguide modes is given by

$$F_{tot,TE} = \int_0^{360^\circ} S_\beta(k_\xi) C_{TE}^2 d\beta, \quad (9)$$

$$F_{tot,TM} = \int_0^{360^\circ} S_\beta(k_\xi) C_{TM}^2 d\beta, \quad (10)$$

where  $S_\beta(k_\xi)$  describes the amplitude and phase information in direction  $\beta$ . The positive  $k_\xi$  axis of  $S_\beta(k_\xi)$  is used for  $0^\circ \leq \beta < 180^\circ$  and the negative for  $180^\circ \leq \beta < 360^\circ$ .

However, for metallic nanodisks we need to consider additional features, namely the particle plasmons. Light with an incident polarisation  $\mathbf{E}_x$  can excite particle plasmons along the principal axes  $u$ ,  $v$ , and  $z$  [see Fig. 2(e)]. This leads to the following components:

$$C_{plu} = C_{\alpha,xy} C_u \cos(\alpha - \gamma), \quad (11)$$

$$C_{plv} = C_{\alpha,xy} C_v \sin(\alpha - \gamma), \quad (12)$$

$$C_{plz} = C_{\alpha,z} C_z. \quad (13)$$

The values  $C_u$ ,  $C_v$ , and  $C_z$  in Eqs. (11) – (13) are dependent on the eccentricity and the size of the particle. The three excited particle plasmons can be considered as independently polarised light, which is incident on the sample. These electric field vectors ( $\mathbf{E}_{plu}$ ,  $\mathbf{E}_{plv}$ , and  $\mathbf{E}_{plz}$ ) can then excite waveguide modes in the same manner as explained above. Figure 2(f) shows how each of the electric field vectors of the particle plasmons  $\mathbf{E}_{plu}$  and  $\mathbf{E}_{plv}$  splits up into a TE polarised as well as a TM polarised wave in direction  $\beta$  leading to the components

$$C_{TEu} = -C_{plu} \sin(\beta - \gamma), C_{TEv} = C_{plv} \cos(\beta - \gamma), \quad (14)$$

$$C_{TEz} = C_{plz},$$

$$C_{TMu} = C_{plu} \cos(\beta - \gamma), C_{TMv} = C_{plv} \sin(\beta - \gamma). \quad (15)$$

As above in Eqs. (5) and (6) for the electric field vector  $\mathbf{E}_{\alpha,z}$ , the particle plasmon in  $z$  direction can only excite a TE polarised waveguide mode. Note the - sign for the  $C_{TEu}$  component which is due to the fact that  $\mathbf{E}_{TEu}$  points in the opposite direction than  $\mathbf{E}_{TEv}$  [Fig. 2(f)]. The complete components  $C_{TE,add}$  and  $C_{TM,add}$  are obtained by adding up the different components of Eqs. (5) and (14) for a TE wave as well as those of Eqs. (6) and (15) for a TM wave in  $\beta$  direction:

$$C_{TE,add} = C_{TE} + C_{TEu} + C_{TEv} + C_{TEz}, \quad (16)$$

$$C_{TM,add} = C_{TM} + C_{TMu} + C_{TMv}. \quad (17)$$

The total intensity of the waveguide modes for metallic nanodisks can now be calculated by using

$$F_{tot,TE} = \int_0^{360^\circ} S_\beta(k_\xi) C_{TE,add}^2 d\beta, \quad (18)$$

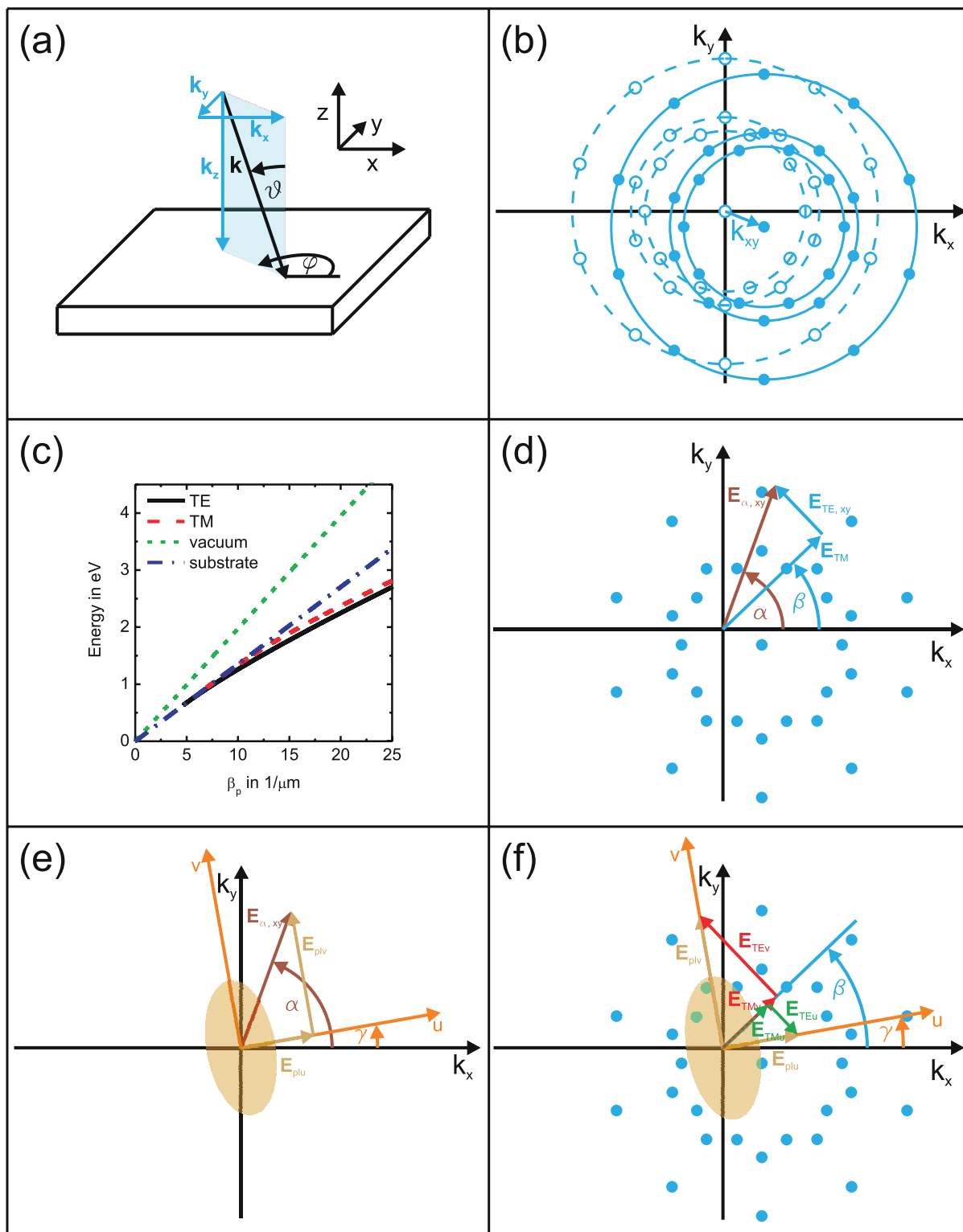


**Figure 2 | Simulation model.** (a) Illustration of the incident  $\mathbf{k}$ -vector on the sample. (b) Angular Fourier transform (filled circles) shifted by  $\mathbf{k}_{xy}$  with respect to the Fourier transform for normal incidence (open circles). (c) Dispersion relations for vacuum (green short-dashed) and quartz (blue dash-dotted) as well as for TE (black solid) and TM waves (red dashed) propagating in a 180-nm-thick  $\text{HfO}_2$  layer on quartz. (d) TE and TM waveguide modes in direction  $\beta$  for incident polarisation  $E_{z,xy}$ . (e) Particle plasmon excitations along the particle main axes. (f) Additionally excited TE and TM waveguide modes in direction  $\beta$  due to the particle plasmons.

$$F_{tot, TM} = \int_0^{360^\circ} S_\beta(k_\xi) C_{TM, add}^2 d\beta. \quad (19)$$

As already explained above, the positive  $k_\xi$  axis of  $S_\beta(k_\xi)$  is used for  $0^\circ \leq \beta < 180^\circ$  and the negative for  $180^\circ \leq \beta < 360^\circ$ .

$F_{tot, TE}$  as well as  $F_{tot, TM}$  consist of amplitudes at specific  $k$  values. The corresponding energies are obtained by using the above-mentioned waveguide mode dispersion relations displayed in Fig. 2(c) as black solid (TE wave) and red dashed (TM wave) curves. As reference also the dispersion relations of the surrounding media are plotted



(vacuum: green short-dashed, quartz: blue dash-dotted). The amplitudes  $A_j$  of the main waveguide mode resonances in Eqs. (18) and (19) at the energies  $E_j$  are used in order to describe the transmission amplitude  $t$  by a Fano model<sup>27,33,34</sup>

$$t = A_{bg} e^{i\phi_{bg}} - \frac{A_{plu} \cos^2(\alpha - \gamma) \Gamma_{plu} e^{i\phi_{plu}}}{E - E_{plu} + i\Gamma_{plu}} - \frac{A_{plv} \sin^2(\alpha - \gamma) \Gamma_{plv} e^{i\phi_{plv}}}{E - E_{plv} + i\Gamma_{plv}} + A \sum_j \frac{-A_j \Gamma_j e^{i\phi_j}}{E - E_j + i\Gamma_j} \quad (20)$$

where the sum over  $j$  models the waveguide modes with spectral widths  $\Gamma_j$  and phase  $\phi_j$ . The first term is due to the directly transmitted wave with amplitude  $A_{bg} = 1$  and phase  $\phi_{bg} = 0.085 \pi$ , whereas the second and third terms describe the particle plasmons in  $u$  and  $v$  directions with amplitudes  $A_{plu}/A_{plv}$ , spectral widths  $\Gamma_{plu}/\Gamma_{plv} = 0.15$  eV, and phases  $\phi_{plu}/\phi_{plv} = \frac{\pi}{2}$ . Note that the particle plasmon in  $z$  direction is neglected since the height of the nano-disk is much smaller than the diameters in  $u$  and  $v$  direction. Therefore, the particle plasmon energy in  $z$  direction is in a different energy range as the measured spectra and the value  $C_z$  of Eq. (13) is much smaller than  $C_u$  and  $C_v$ . The amplitudes  $A_{plu}$  and  $A_{plv}$  as well as the value  $A$  are fitting parameters so that the particle plasmon amplitudes and the waveguide mode amplitudes possess the correct ratio. The phase of a waveguide mode not coupled to a particle plasmon is  $\phi_\infty = 0.47 \pi$ , which is the case when the energy of the waveguide mode is far away from the particle plasmon energy. For low energies the phase of the waveguide mode  $\phi_j$  converges to  $\phi_\infty$ , whereas for large energies it converges to  $\phi_\infty + 2\pi$  which corresponds to  $\phi_\infty$ . If waveguide mode and particle plasmon possess the same energy,  $\phi_j$  has a phase-shift of  $\pi$  with respect to the uncoupled phase  $\phi_\infty$ . Therefore, a phase behaviour of

$$\begin{aligned} \varphi_j = & 2 \arctan \left( \frac{E - E_{plu}}{2\Gamma_{plu}} \right) \cos^2(\alpha - \gamma) \\ & + 2 \arctan \left( \frac{E - E_{plv}}{2\Gamma_{plv}} \right) \sin^2(\alpha - \gamma) + \phi_\infty + \pi \end{aligned} \quad (21)$$

is assumed due to the two particle plasmons at energies  $E_{plu}$  and  $E_{plv}$ . The extinction spectra can then be obtained by calculating  $\text{Ext} = -\ln(T)$  with the transmittance  $T = |t|^2$ .

**Experiments.** The sample described in the **Methods** section was fabricated and then measured with a white light transmission setup<sup>15</sup>. The measurement principle is also described in the **Methods** section. The angle of incidence  $\vartheta$  was varied between  $0^\circ$  and  $6^\circ$  in steps of  $1^\circ$  both in  $x$  ( $\varphi = 0^\circ$ ) and in  $y$  direction ( $\varphi = 90^\circ$ ) of the sample. All measurements, shown as black curves in Figs. 3 and 4, were performed for an incident polarisation with  $\alpha = 0^\circ$  and  $\alpha = -90^\circ$ , respectively. The curves on the bottom of Fig. 3(a) and (b) as well as those of Fig. 4(a) and (b) were measured at normal light incidence. The broad resonances visible in all spectra without the dips are the excited particle plasmons. Due to the fact that the short main axis of the gold disks is rotated by  $40^\circ$  around the sample  $x$  axis, the particle plasmon resonances along both main axes are excited for incident polarisations with  $\alpha = 0^\circ$  and  $\alpha = -90^\circ$ . However, by comparing Fig. 3 to Fig. 4, one recognises that the particle plasmons are located at slightly different energies. This means that either the plasmon along the short main axis (Fig. 3) or the plasmon along the long main axis (Fig. 4) is more pronounced. The sharp resonances at approximately 1.5 eV, 1.6 eV, 1.75 eV, and 1.85 eV are due to TE and TM waveguide modes propagating in the waveguide layer with a propagation constant equal to the inner ring of the Fourier components [see inner dashed circle in Fig. 2(b)] as well as those with a propagation constant equal to the outer ring of the Fourier components [see central dashed circle in

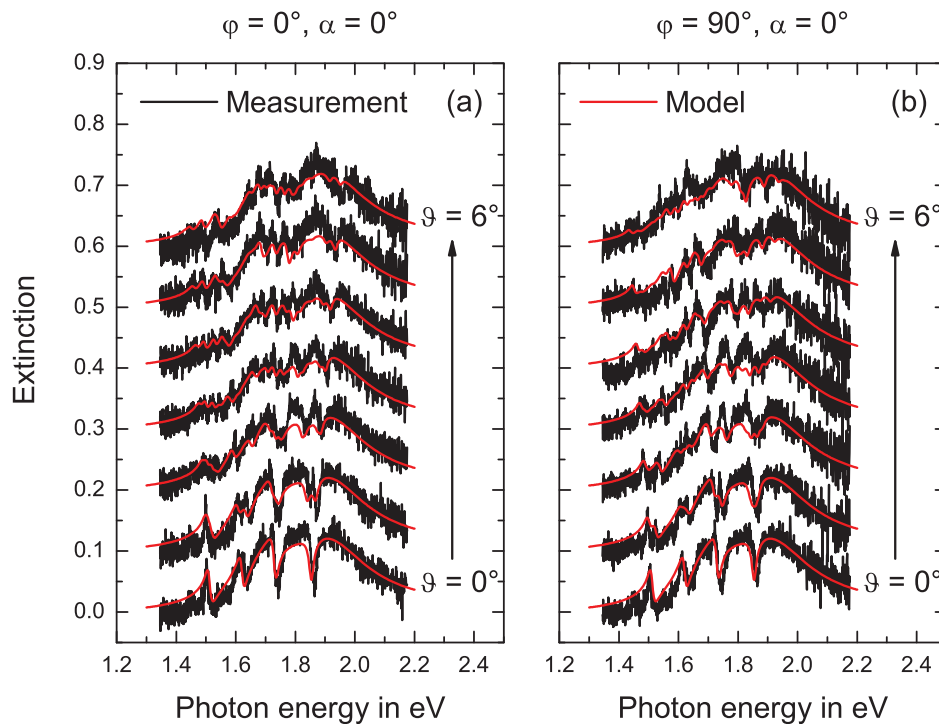


**Figure 3** | Measurements with polarisation  $\alpha = 0^\circ$ . Measured (black) and modelled (red) curves for a Penrose tiling with edge length  $d = 530$  nm. The angle of incidence was varied from  $0^\circ$  to  $6^\circ$  (from bottom to top) (a) along the sample  $x$  direction ( $\varphi = 0^\circ$ ) and (b) along the sample  $y$  direction ( $\varphi = 90^\circ$ ). The incident polarisation was  $0^\circ$ . The curves are shifted upward for clarity.

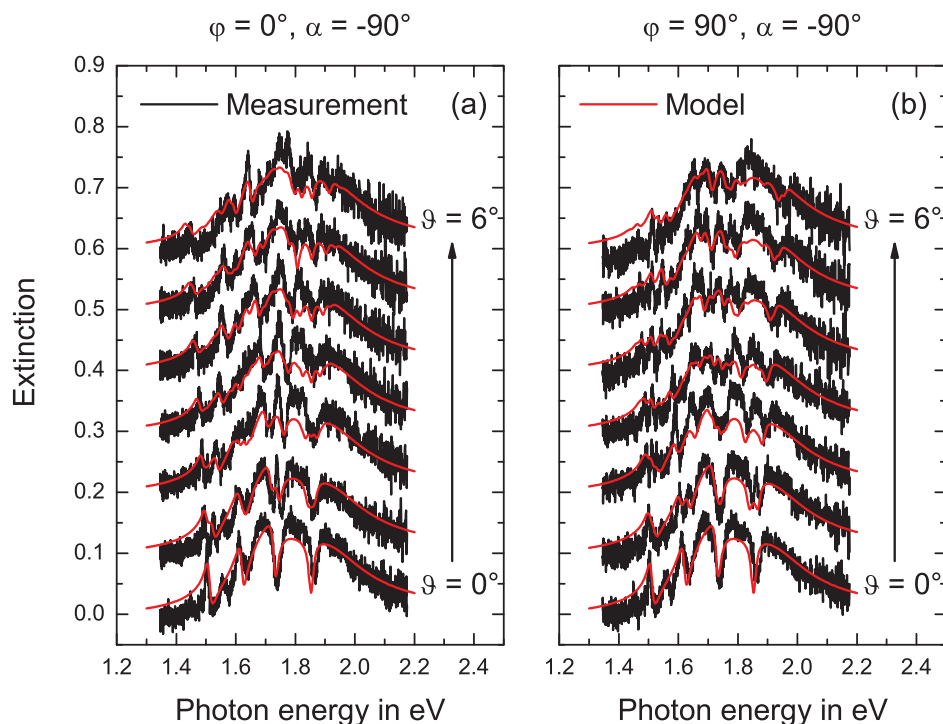


**Figure 4** | Measurements with polarisation  $\alpha = -90^\circ$ . Measured (black) and modelled (red) curves for a Penrose tiling with edge length  $d = 530$  nm. The angle of incidence was varied from  $0^\circ$  to  $6^\circ$  (from bottom to top) (a) along the sample  $x$  direction ( $\varphi = 0^\circ$ ) and (b) along the sample  $y$  direction ( $\varphi = 90^\circ$ ). The incident polarisation was  $-90^\circ$ . The curves are shifted upward for clarity.

Fig. 2(b)]. According to the energy position of the waveguide modes compared to the particle plasmons and thus to the degree of coupling between these resonances, the waveguide modes either appear as sharp peaks (decoupled, see resonance at 1.5 eV) or as sharp dips (coupled, see resonance at 1.85 eV). By tilting the sample, the waveguide modes split up into different components<sup>16,30</sup> due to the different absolute values of the propagation constants for oblique light incidence. The behaviour for varying the inclination angle in  $x$  direction is different than that in  $y$  direction as expected. Additionally, we observe that this behaviour is dependent on the incident polarisation. This polarisation dependence has two reasons. First, the waveguide modes directly excited by the incident light show the same resonances with the same amplitudes for all spectra with  $\alpha = \varphi = 0^\circ, 36^\circ, 72^\circ, 108^\circ \dots$ . The location as well as the amplitudes of these waveguide modes differ from the spectra with  $\alpha = \varphi = 18^\circ, 54^\circ, 90^\circ, 126^\circ \dots$  due to the 10-fold symmetry of the Penrose tiling. Second, due to the fact that there are also waveguide modes present in the system that are excited by the particle plasmons, the amplitudes of the waveguide modes are also different for the spectra with for example  $\alpha = \varphi = 0^\circ$  and  $\alpha = \varphi = 36^\circ$ . However, the differences due to the second reason are only present, when the gold dots are elliptically shaped. The red curves in Figs. 3 and 4 are the spectra calculated with the simulation model presented in subsection **Modelling and Simulations**. A measured curve for one polarisation at normal light incidence was taken for fitting the theoretical spectrum to it. The fitting parameters obtained there were  $A_{plu} = 0.0735$ ,  $A_{plv} = 0.1129$ , and  $A = 0.0016$  and were used for calculating all other spectra. By comparing the measured and modelled spectra of Fig. 3, we observe an excellent agreement for both  $x$  and  $y$  variation of the inclination angle. The behaviour of the measured spectra of incident polarisation angle  $\alpha = -90^\circ$  (see Fig. 4) with the same fitting parameters is also well reproduced by the calculated spectra which confirms our model. Measured and modelled curves are shown here for incidence angles up to  $6^\circ$ . However, our model can easily predict the optical properties at larger angles.

## Discussion

We have introduced a theoretical model for simulating the optical properties of 2D metallic photonic quasicrystals at normal and oblique light incidence for all polarisations. This model includes the Fourier transform of the structure shifted by the  $k$  vector component parallel to the structure surface and all possible waveguide modes as well as particle plasmon resonances. The energy spectrum is obtained by utilising the waveguide dispersion relations and a phenomenological model. We have measured a quasicrystalline plasmonic crystal sample by varying the angle of incidence as well as the light polarisation and obtained excellent agreement between the measured and the modelled spectra. Our model could find applications in plasmonic quasicrystalline super-oscillatory lenses<sup>35</sup> as well as plasmonically enhanced solar cells using waveguide-plasmon geometries<sup>23,36</sup>.

## Methods

**Fabrication.** The quasiperiodic lattice of the measured sample consists of 25-nm-high gold nanodisks which were placed on the vertices of a Penrose tiling with an edge length of 530 nm by using electron beam lithography. This arrangement is depicted in Fig. 1. Quartz ( $n = 1.46$ ) with a 180-nm-thick  $\text{HfO}_2$  waveguide layer on top served as substrate. The refractive index of  $\text{HfO}_2$  is dispersive in the relevant spectral range and can be described by the following equation:

$$n = 1.905 + \frac{0.021}{\lambda^2} - \frac{0.0003}{\lambda^4} \quad (22)$$

with  $\lambda$  as the wavelength of the incident light in  $\mu\text{m}$ . The gold disks are elliptically shaped (97 nm and 118 nm long main axis diameters) and rotated by an angle of  $40^\circ$  between the short main axis of the particle and the sample  $x$  axis.

**Measurements.** The light of a white light source was polarised and then focused on the sample by using a microscope objective (Zeiss, A-Plan, 10x, 0.25). The polariser was mounted on a rotation stage in order to change the incident polarisation. The light behind the sample was collimated and then focused on the slit of a spectrometer (Acton SpectraPro 500i with a CCD camera and a grating with 150 g/mm). A pinhole was used in the collimated beam after the sample in order to reduce the aperture angle of the beam below  $0.2^\circ$ <sup>15</sup>. The sample was placed on a rotation stage in order to perform measurements with different incidence angles on the sample.



1. Lal, S., Link, S. & Halas, N. J. Nano-optics from sensing to waveguiding. *Nat. Phot.* **1**, 641–648 (2007).
2. Liu, N., Mesch, M., Weiss, T., Hentschel, M. & Giessen, H. Infrared perfect absorber and its application as plasmonic sensor. *Nano Lett.* **10**, 2342–2348 (2010).
3. Yanik, A. A., Huang, M., Artar, A., Chang, T.-Y. & Altug, H. Integrated nanoplasmonic-nanofluidic biosensors with targeted delivery of analytes. *Appl. Phys. Lett.* **96**, 021101 (2010).
4. Luk'yanchuk, B. *et al.* The fano resonance in plasmonic nanostructures and metamaterials. *Nat. Mater.* **9**, 707–715 (2010).
5. Lamprecht, B. *et al.* Metal nanoparticle gratings: Influence of dipolar particle interaction on the plasmon resonance. *Phys. Rev. Lett.* **84**, 4721–4724 (2000).
6. Auguie, B. & Barnes, W. L. Collective resonances in gold nanoparticle arrays. *Phys. Rev. Lett.* **101**, 143902 (2008).
7. García-Vidal, F. J., Martín-Moreno, L., Ebbesen, T. W. & Kuipers, L. Light passing through subwavelength apertures. *Rev. Mod. Phys.* **82**, 729–787 (2010).
8. Matsui, T., Agrawal, A., Nahata, A. & Vardeny, Z. V. Transmission resonances through aperiodic arrays of subwavelength apertures. *Nature* **446**, 517–521 (2007).
9. Rockstuhl, C., Lederer, F., Zentgraf, T. & Giessen, H. Enhanced transmission of periodic, quasiperiodic, and random nanoaperture arrays. *Appl. Phys. Lett.* **91**, 151109 (2007).
10. Zoorob, M. E., Charlton, M. D. B., Parker, G. J., Baumberg, J. J. & Netti, M. C. Complete photonic bandgaps in 12-fold symmetric quasicrystals. *Nature* **404**, 740–743 (2000).
11. Prikulis, J., Hanarp, P., Olofsson, L., Sutherland, D. & Käll, M. Optical spectroscopy of nanometric holes in thin gold films. *Nano Lett.* **4**, 1003–1007 (2004).
12. Ledermann, A. *et al.* Three-dimensional silicon inverse photonic quasicrystals for infrared wavelengths. *Nat. Mater.* **5**, 942–945 (2006).
13. Ledermann, A., Wegener, M. & von Freymann, G. Rhombicuboctahedral three-dimensional photonic quasicrystals. *Adv. Mater.* **22**, 2363–2366 (2010).
14. Linden, S., Kuhl, J. & Giessen, H. Controlling the interaction between light and gold nanoparticles: Selective suppression of extinction. *Phys. Rev. Lett.* **86**, 4688–4691 (2001).
15. Christ, A., Tikhodeev, S., Gippius, N. A., Kuhl, J. & Giessen, H. Waveguide-plasmon polaritons: Strong coupling of photonic and electronic resonances in a metallic photonic crystal slab. *Phys. Rev. Lett.* **91**, 183901 (2003).
16. Christ, A. *et al.* Optical properties of planar metallic photonic crystal structures: Experiment and theory. *Phys. Rev. B* **70**, 125113 (2004).
17. Nau, D. *et al.* Disorder issues in metallic photonic crystals. *phys. stat. sol. (b)* **243**, 2331–2343 (2006).
18. Hughes, S., Ramunno, L., Young, J. F. & Sipe, J. E. Extrinsic optical scattering loss in photonic crystal waveguides: Role of fabrication disorder and photon group velocity. *Phys. Rev. Lett.* **94**, 033903 (2005).
19. Cao, H. *et al.* Spatial confinement of laser light in active random media. *Phys. Rev. Lett.* **84**, 5584–5587 (2000).
20. Zentgraf, T., Christ, A., Kuhl, J. & Giessen, H. Tailoring the ultrafast dephasing of quasiparticles in metallic photonic crystals. *Phys. Rev. Lett.* **93**, 243901 (2004).
21. Utikal, T., Stockman, M. I., Heberle, A. P., Lippitz, M. & Giessen, H. All-optical control of the ultrafast dynamics of a hybrid plasmonic system. *Phys. Rev. Lett.* **104**, 113903 (2010).
22. Utikal, T. *et al.* Towards the origin of the nonlinear response in hybrid plasmonic systems. *Phys. Rev. Lett.* **106**, 133901 (2011).
23. Pala, R. A., White, J., Barnard, E., Liu, J. & Brongersma, M. L. Design of plasmonic thin-film solar cells with broadband absorption enhancements. *Adv. Mater.* **21**, 3504–3509 (2009).
24. Spinelli, P. *et al.* Optical impedance matching using coupled plasmonic nanoparticle arrays. *Nano Lett.* **11**, 1760–1765 (2011).
25. Huang, F. M., Zheludev, N., Chen, Y. & García de Abajo, F. J. Focusing of light by a nanohole array. *Appl. Phys. Lett.* **90**, 091119 (2007).
26. Florescu, M., Torquato, S. & Steinhardt, P. J. Complete band gaps in two-dimensional photonic quasicrystals. *Phys. Rev. B* **80**, 155112 (2009).
27. Bauer, C., Kobiela, G. & Giessen, H. Optical properties of two-dimensional quasicrystalline plasmonic arrays. *Phys. Rev. B* **84**, 193104 (2011).
28. Kak, A. C. & Slaney, M. *Principles of Computerized Tomographic Imaging*. IEEE Press (1988).
29. Mersereau, R. M. & Oppenheim, A. V. Digital reconstruction of multidimensional signals from their projections. *Proc. IEEE* **62**, 1319–1338 (1974).
30. Linden, S., Christ, A., Kuhl, J. & Giessen, H. Selective suppression of extinction within the plasmon resonance of gold nanoparticles. *Appl. Phys. B* **73**, 311–316 (2001).
31. Tien, P. K. Light waves in thin films and integrated optics. *Appl. Opt.* **10**, 2395–2413 (1971).
32. Kogelnik, H. & Ramaswamy, V. Scaling rules for thin-film optical waveguides. *Appl. Opt.* **13**, 1857–1862 (1974).
33. Fan, S. & Joannopoulos, J. D. Analysis of guided resonances in photonic crystal slabs. *Phys. Rev. B* **65**, 235112 (2002).
34. Christ, A. *et al.* Controlling the fano interference in a plasmonic lattice. *Phys. Rev. B* **76**, 201405(R) (2007).
35. Rogers, E. T. F. *et al.* A super-oscillatory lens optical microscope for subwavelength imaging. *Nat. Mater.* **11**, 432–435 (2012).
36. Atwater, H. A. & Polman, A. Plasmonics for improved photovoltaic devices. *Nat. Mater.* **9**, 205–213 (2010).

## Acknowledgments

The authors thank T. Weiss, J. Roth, P. Köberle, S. Tikhodeev, and C. Bechinger for useful discussions and suggestions. This work was financially supported by Deutsche Forschungsgemeinschaft (Open Access Publishing, SPP1391 and FOR557), by Landesstiftung BW, and by BMBF (13N9155 and 13N10146).

## Author contributions

C.B. fabricated the sample, developed the simulation model, and carried out the measurements. G.K. helped developing the model. C.B. and H.G. wrote the manuscript. All authors contributed to scientific discussion and critical revision of the article. H.G. supervised the study.

## Additional information

**Competing financial interests:** The authors declare no competing financial interests.

**License:** This work is licensed under a Creative Commons Attribution-NonCommercial-NoDerivs 3.0 Unported License. To view a copy of this license, visit <http://creativecommons.org/licenses/by-nc-nd/3.0/>

**How to cite this article:** Bauer, C., Kobiela, G. & Giessen, H. 2D quasiperiodic plasmonic crystals. *Sci. Rep.* **2**, 681; DOI:10.1038/srep00681 (2012).